inorganics

MDPI

Article

Carbon-Based $Sb_2(S, Se)_3$ Solar Cells

Yue Deng [1], Huicong Liu [1], Hailiang Wang [1], Yongfa Song [1], Weiping Li [1], Liqun Zhu [1], Xiangfan Xie [2], Shuang Xiao [2,*] and Haining Chen [1,*]

[1] School of Materials Science and Engineering, Beihang University, No. 37 Xueyuan Road, Haidian District, Beijing 100191, China
[2] Shenzhen Key Laboratory of Ultra-Intense Laser and Advanced Material Technology, Center for Advanced Material Diagnostic Technology, College of Engineering Physics, Shenzhen Technology University, Shenzhen 518118, China
* Correspondence: xiaoshuang@sztu.edu.cn (S.X.); chenhaining@buaa.edu.cn (H.C.)

Abstract: $Sb_2(S, Se)_3$ solar cells have shown great promise due to the advantages of low cost, non-toxic and high stability. However, traditional devices commonly use noble metal as the back electrode, which not only increases device cost but also limits device stability. Herein, carbon materials are used to replace the noble metals in $Sb_2(S, Se)_3$ solar cells. In addition, to grow high-quality $Sb_2(S, Se)_3$ films, a two-step hydrothermal method was developed. The carbon-based $Sb_2(S, Se)_3$ solar cells based on the above film achieved a power conversion efficiency (PCE) of 2.76%. After inserting a stable P3HT layer at the $Sb_2(S, Se)_3$ film/carbon interface, hole extraction was enhanced and the PCE was promoted to 4.15%. This work brings out a promising route to produce emerging solar cells with cost-effective and stable materials.

Keywords: solar cell; carbon electrode; antimony selenide; charge extraction

Citation: Deng, Y.; Liu, H.; Wang, H.; Song, Y.; Li, W.; Zhu, L.; Xie, X.; Xiao, S.; Chen, H. Carbon-Based $Sb_2(S, Se)_3$ Solar Cells. *Inorganics* **2023**, *11*, 159. https://doi.org/10.3390/inorganics11040159

Academic Editor: Catherine Housecroft

Received: 29 November 2022
Revised: 28 March 2023
Accepted: 5 April 2023
Published: 8 April 2023

1. Introduction

Semiconducting metal chalcogenides have reached notable achievements as absorbers in photovoltaic modules [1]. As the representative, cadmium telluride (CdTe) solar cells have overcome the power conversion efficiency (PCE) of 22% [1]. However, Te reserves are rather low on Earth, and Cd is highly toxic, which seriously restricts its application [2–4]. Therefore, it is necessary to develop earth-abundant and non-toxic materials as alternative light absorbers. Among various metal chalcogenides, $Sb_2(S, Se)_3$ has attracted more and more attention in recent years because of its optimal bandgap (1.1~1.7 eV), high absorption coefficient (>10^5 cm), and excellent stability [3–5]. So far, great progress has been made on $Sb_2(S, Se)_3$ solar cells [2,4–7]. Chen et al. have successfully developed a one-step hydrothermal method to grow high-quality $Sb_2(S, Se)_3$ film with the device structure of FTO/CdS/$Sb_2(S, Se)_3$/Spiro-OMeTAD/Au, which promoted the PCE to over 10% [4].

However, the best-performed devices required Spiro-OMeTAD as the hole transport material (HTM), which has several drawbacks in terms of commercialization [4,6]. The synthesis of Spiro-OMeTAD involves several complex reactions, which require harsh conditions (−78 °C) and aggressive reagents (Br_2) [8,9]. Its total yield is less than 30% when synthesized from commercially available raw materials. In addition, highly pure sublimation-grade Spiro-OMeTAD is required to fabricate high-performance solar cells. The result is that its price has surpassed USD 100 per gram, which is too expensive for large-scale usage [6]. Furthermore, Spiro-OMeTAD needs hygroscopic dopants to improve its conductivity, which accelerates the degradation of solar cells [10,11]. Similarly, a dithieno [3,2-b:2′,3′-d] pyrrole-cored small molecule (DTPThMe-ThTPA) has proved to be another efficient HTM. However, it also needs Li-TFSI dopants and the cost for the synthesis of DTPThMe-ThTPA is still relatively high, around USD 20 per gram [6]. The HTM-free $Sb_2(S, Se)_3$ solar cells showed much better stability than the ones employing doped Spiro-OMeTAD [4]. For the counter electrode materials, precious metals, such as gold, were

commonly used for $Sb_2(S, Se)_3$ solar cells. These need to be deposited in a vacuum, which further pushed up the fabrication costs [3,4,6]. These unsolved problems of low stability and high cost seriously hamper the industrial application of $Sb_2(S, Se)_3$ in photovoltaics. In this regard, stable and low-cost HTMs and electrode materials are in strong demand.

Poly(3-hexylthiophene) (P3HT) is an alternative polymer HTM with outstanding optoelectronic properties [12,13]. It needs 3 steps to be synthesized with over 60% total yield, which means its cost-per-gram is relatively low among various organic HTMs [13,14]. Aside from these, it could be directly used in solar cells without dopants, which benefits its stability [10]. For the counter electrode materials, carbon materials have a work function of ~5 eV, which is close to the work function of Au (~4.6 eV) [15–17]. Furthermore, they have remarkable advantages in abundance, price competence, and stability, which make them an excellent option as a counter electrode for solar cells [15]. In this way, developing $Sb_2(S, Se)_3$ solar cells with the discussed materials should be highly promising to reduce fabrication costs.

Herein, $Sb_2(S, Se)_3$ solar cells were fabricated with carbon materials as counter electrodes and P3HT as HTM. Since both P3HT and carbon electrodes commonly show poorer hole selectivity, a two-step hydrothermal method was developed to grow high-quality $Sb_2(S, Se)_3$ films with a composition and energy level gradient, which would help to enhance hole extraction and charge separation. In detail, Sb_2S_3 and $Sb_2(S, Se)_3$ films were subsequently deposited on a substrate by hydrothermal methods. Then, we employed carbon materials as the counter electrodes and named $Sb_2(S, Se)_3$ solar cells without HTMs and precious metal electrodes as carbon-based $Sb_2(S, Se)_3$ solar cells. The carbon-based $Sb_2(S, Se)_3$ solar cells could achieve a PCE of 2.76%. Furthermore, by inserting a P3HT layer between the $Sb_2(S, Se)_3$ film and carbon electrode, hole extraction was significantly enhanced and the PCE was improved to 4.15%.

2. Results and Discussion

As stated above, constructing a suitable energy level gradient via forming a composition gradient could favor hole extraction. However, it is hard to grow a $Sb_2(S, Se)_3$ layer with a composition gradient by the conventional one-step hydrothermal method. Therefore, in our present work, a two-step hydrothermal method was developed to control the composition gradient. The whole procedure was illustrated in Figure 1. A Sb_2S_3 layer was firstly grown on the pre-deposited FTO/SnO_2/CdS substrate by the hydrothermal method in the solution containing $KSbC_4H_4O_7 \cdot 0.5H_2O$ and $Na_2S_2O_3 \cdot 5H_2O$. In the second step, selenourea was added to the solution as a Se source for the deposition of the $Sb_2(S, Se)_3$ layer, and the deposited Sb_2S_3 layer was used as substrate. Finally, the stacked films were annealed at 350 °C for 15 min in a glove box filled with N_2 to get the final targeted films.

Scanning electron microscopy (SEM) images were taken to characterize the change in the morphology of different films. As shown in Figure 2a, the Sb_2S_3 film exhibited a flat surface with a large grain size (2~3.5 μm), while many pinholes could also be observed. After the introduction of Se (Figure 2b), the $Sb_2(S, Se)_3$ film displayed a much smaller grain size (about 0.5~2 μm) than that of the Sb_2S_3 film and showed no pinholes. Furthermore, the surface of the $Sb_2(S, Se)_3$ film was significantly rougher than that of the Sb_2S_3 (Figure 2d,e) film. Surprisingly, when Sb_2S_3 film was used as the substrate for the growth of the $Sb_2(S, Se)_3$ film, the $Sb_2S_3/Sb_2(S, Se)_3$ film exhibited a flat surface, large grains, and small pinholes, which combined the advantages of Sb_2S_3 films and $Sb_2(S, Se)_3$ films (Figure 2c). Different from the surface morphology, the thicknesses of the three films were similar, around 400 nm (Figure 2d–f), indicating that the nucleation rate of Sb_2S_3 on CdS film was smaller than that of $Sb_2(S, Se)_3$ [17,18]. In addition, the nucleation rate of $Sb_2(S, Se)_3$ on CdS film was larger than that on Sb_2S_3 film. As Figure S1 shows, the hydrothermal reaction time of Sb_2S_3 remarkably affected the morphology of $Sb_2S_3/Sb_2(S, Se)_3$ films. As the reaction time increased, the grains of $Sb_2S_3/Sb_2(S, Se)_3$ films enlarged from ~3 μm to tens of micrometers, which indicates that the morphology of Sb_2S_3 films also affects the nucleation rate of $Sb_2(S, Se)_3$. It has been reported that morphological ordering of compact and large grain size is an

important factor in enhancing the performance of thin film solar cells [19]. Although the longer growth time of Sb_2S_3 films enabled larger grains of stacked films, cracks began to appear on the surface of $Sb_2S_3/Sb_2(S, Se)_3$ films grown on Sb_2S_3 substrate with a reaction time of 4 h (Figure S1d). The crack is a kind of defect in semiconductors, which should be avoided to reach high-performance solar cells [14].

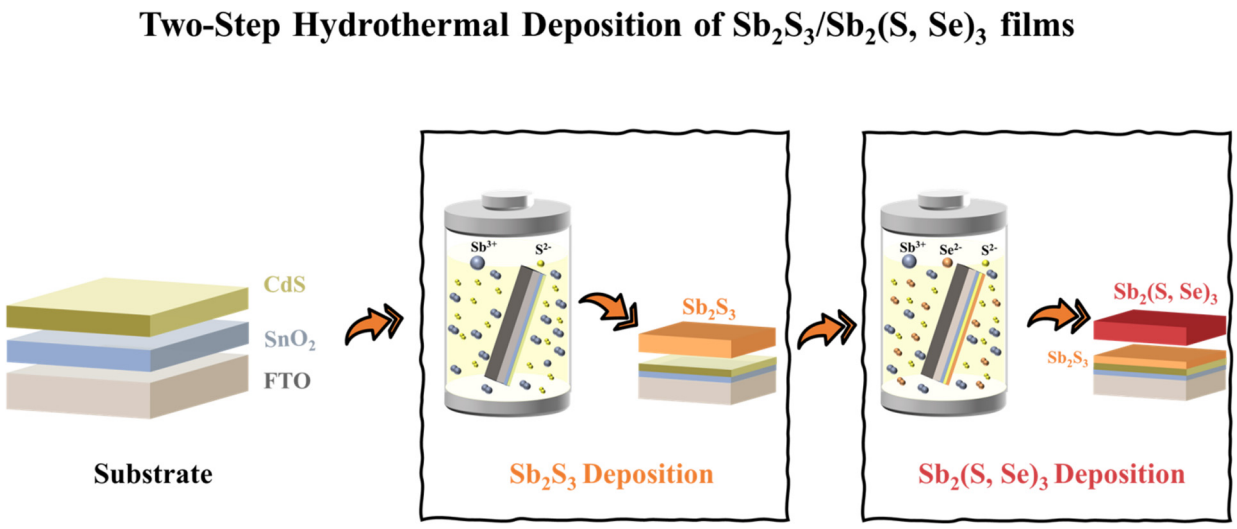

Figure 1. Schematic illustration of the two-step hydrothermal deposition of $Sb_2S_3/Sb_2(S, Se)_3$ films. The Sb_2S_3 layer was first deposited on FTO/SnO_2/CdS substrate followed by the deposition of the $Sb_2(S, Se)_3$ layer.

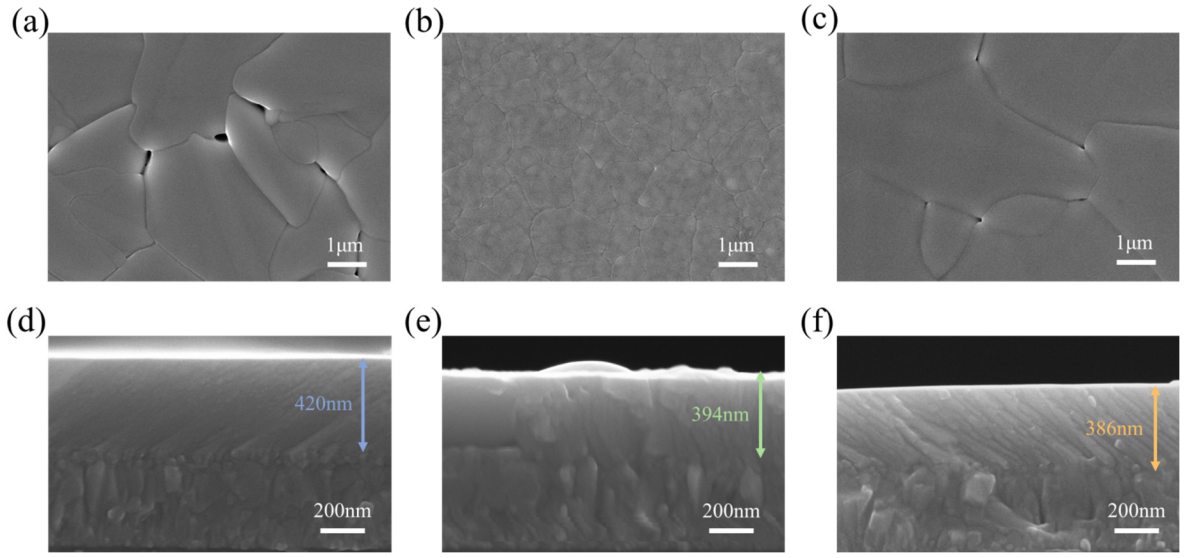

Figure 2. Top-view SEM images of the (**a**) Sb_2S_3, (**b**) $Sb_2(S, Se)_3$, and (**c**) $Sb_2S_3/Sb_2(S, Se)_3$ films deposited on FTO/SnO_2/CdS substrates. Corresponding cross-sectional SEM images of (**d**) Sb_2S_3, (**e**) $Sb_2(S, Se)_3$, and (**f**) $Sb_2S_3/Sb_2(S, Se)_3$ films.

X-ray diffraction (XRD) patterns were recorded to characterize the crystal structures of different films. As depicted in Figure 3a, almost all the major diffraction peaks of the Sb_2S_3 film could be indexed to the characteristic peaks of standard Sb_2S_3, indicating its existence in all kinds of films [20]. After selenourea was introduced to precursors, XRD patterns correspondingly shifted toward a low diffraction angle for the $Sb_2(S, Se)_3$ film, which is due to the incorporation of the large Se^{2-} ion (Figure 3b,c). For the $Sb_2S_3/Sb_2(S, Se)_3$ film, the deposition of the $Sb_2(S, Se)_3$ film on the Sb_2S_3 film also slightly shifted the XRD peak positions toward lower diffraction angles, indicating the successful incorporation of Se^{2-}

ions (also see Figure S2). The energy dispersive spectroscopy (EDS) results (Figure S3) showed that the Se/(S + Se) in the Sb_2S_3, $Sb_2(S, Se)_3$ and $Sb_2S_3/Sb_2(S, Se)_3$ films were 0, 23.70% and 20.81%, respectively, which was consistent with the XRD results. As shown in Figure 3e, the texture coefficient of (221) peaks $(TC_{(221)})/TC_{(120)}$ ratio of Sb_2S_3, $Sb_2(S, Se)_3$ and $Sb_2S_3/Sb_2(S, Se)_3$ films were calculated to be 0.75, 1.15 and 1.22, respectively. As reported in the literature, Se introduction could increase the $TC_{(221)}/TC_{(120)}$ ratio, which indicates that $(Sb_4Se_6)_n$ ribbons grow more perpendicular to the substrate [3]. A larger $TC_{(221)}/TC_{(120)}$ ratio yields small series resistance and thus higher PCE. Therefore, the crystal orientation in the $Sb_2S_3/Sb_2(S, Se)_3$ film is the most promising one among the three films.

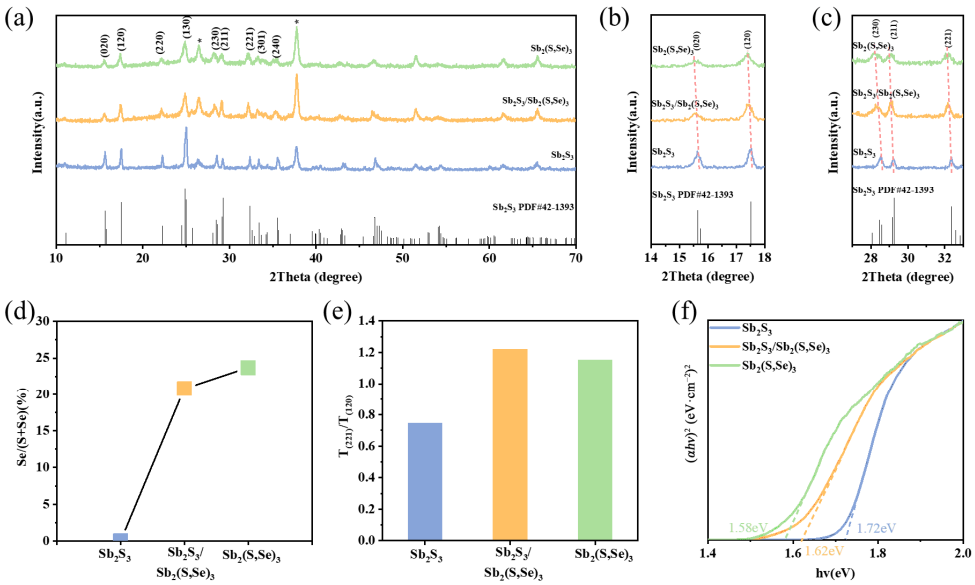

Figure 3. (**a**) XRD patterns of Sb_2S_3, $Sb_2(S, Se)_3$, and $Sb_2S_3/Sb_2(S, Se)_3$ films deposited on FTO/SnO_2/CdS substrates. Asterisks (*) index the peaks of FTO. Corresponding XRD patterns in the 2θ range of (**b**) 14°~18° and (**c**) 27°~33°. (**d**) Se/(S + Se) ratios of different films, which were derived from EDS data. (**e**) $TC_{(221)}/TC_{(120)}$ ratios of different films. (**f**) Tauc plots calculated from UV-vis absorption spectra for different films.

Ultraviolet–visible (UV-vis) spectra were examined to explore the light absorption property of different films. According to the Tauc plots (Figure 3f), the bandgap (E_g) of the Sb_2S_3 film is calculated to be 1.72 eV. After the introduction of Se, the E_g of the $Sb_2(S, Se)_3$ film is reduced to about 1.58 eV. For the $Sb_2S_3/Sb_2(S, Se)_3$ films, the E_g is calculated to be about 1.62 eV, which is between the E_g of $Sb_2(S, Se)_3$ film and the E_g of Sb_2S_3 film.

Carbon electrodes with a thickness of tens of micrometers were directly deposited by painting a commercial carbon paste on the $Sb_2(S, Se)_3$ films followed by annealing treatment at 120 °C for 30 min. Figure 4a shows the scheme of carbon-based $Sb_2(S, Se)_3$ solar cells with the structure of FTO/SnO_2/CdS/$Sb_2(S, Se)_3$/Carbon. A corresponding cross-sectional SEM image of the carbon-based $Sb_2(S, Se)_3$ solar cells indicates that their interfaces are in intimate contact. Current density–voltage (J–V) curves under standard AM 1.5G illumination with the light intensity of 100 mW/cm^2 were measured and the statistical data of photovoltaic parameters were shown in Figure 4b–e. The Sb_2S_3 solar cells displayed a low average PCE (0.65%), with an average open circuit voltage (V_{OC}) of 0.519 V, short circuit current density (J_{SC}) of 5.78 mA·cm^{-2}, and fill factor (FF) of 0.218. For the $Sb_2(S, Se)_3$ solar cells, the average PCE increased to 1.63%. Though the smaller E_g would lead to a lower V_{OC} (0.470 V) than the V_{OC} of Sb_2S_3 solar cells, the enhancement in light utilization promoted the J_{SC} to 11.41 mA·cm^{-2}, which mainly contributed to the improvement of PCE [21,22]. The $Sb_2S_3/Sb_2(S, Se)_3$ solar cells exhibited the highest average PCE of 2.61% among 3 kinds of materials, with a V_{OC} of 0.492 V, J_{SC} of 12.28 mA·cm^{-2} and FF of 0.432. The improved PCE is mainly benefited from the enhanced FF, which is

significantly influenced by the charge extraction of solar cells. The gradient structure of $Sb_2S_3/Sb_2(S, Se)_3$ yields a gradient band alignment, which is believed to accelerate the charge extraction within it [14,20,23,24].

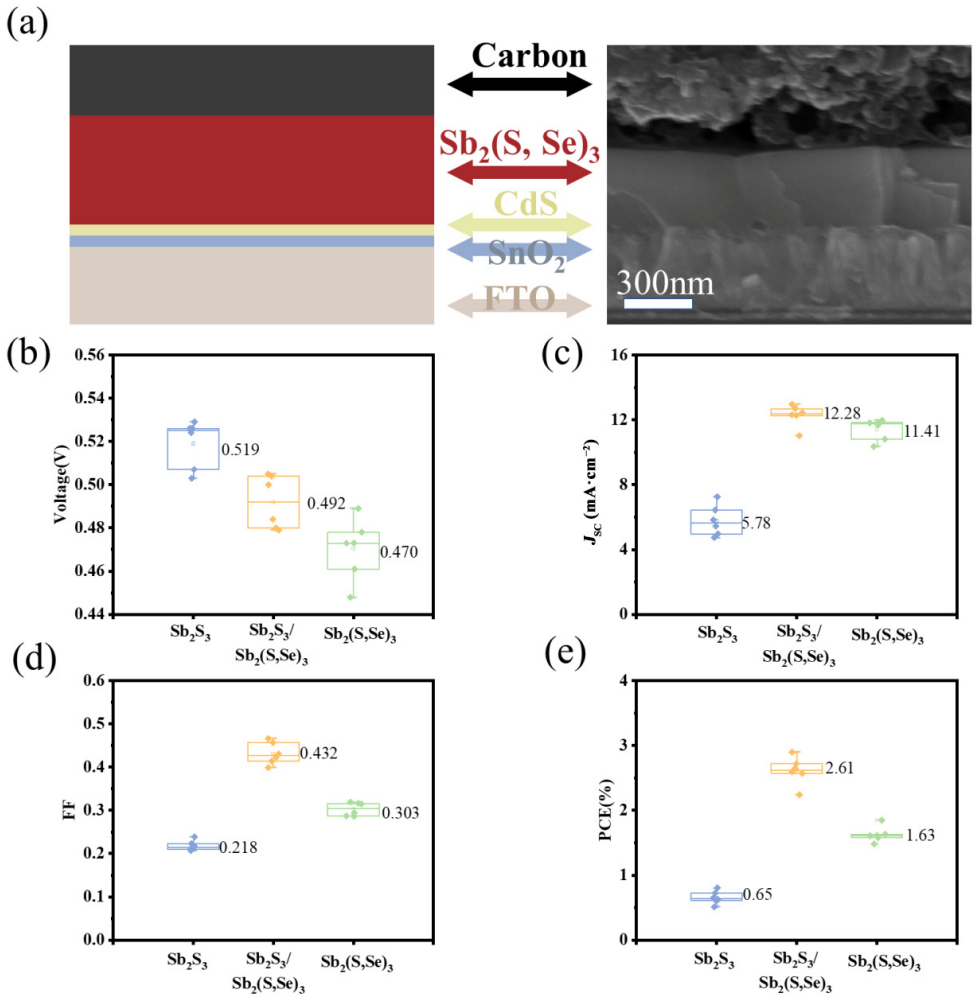

Figure 4. (**a**) Scheme and cross-sectional SEM image of carbon-based $Sb_2(S, Se)_3$ solar cells without HTM. Statistical data obtained from the Sb_2S_3, $Sb_2(S, Se)_3$, and $Sb_2S_3/Sb_2(S, Se)_3$ solar cells: (**b**) V_{OC}, (**c**) J_{SC}, (**d**) FF, and (**e**) PCE.

To further reinforce hole extraction, the stable and cost-effective HTM, P3HT, was employed as an interlayer between the $Sb_2S_3/Sb_2(S, Se)_3$ film and carbon electrode. As previously reported, the strong chemical interaction between P3HT and antimony chalcogenide poses a potential to essentially promote the charge transfer efficiency (Figure 5a) [6]. Raman spectra in Figure 5b indicate that the $Sb_2S_3/Sb_2(S, Se)_3$ film shows the characteristic Sb–S bond vibration at around 307 cm^{-1}, while the peak around 201cm^{-1} is recognized as the characteristic Sb–Se bond vibration [6,25,26]. After P3HT had been added to the solar cells, these chemical bonds became weaker, indicating the existence of interfacial interaction. The adjacent thiophene fractions have chelation towards Sb atoms to form a stable compound, which could displace these Sb-chalcogen bonds to passivate the interfaces. X-ray photoelectron spectroscopy (XPS) was also executed to deeply investigate the passivation effect. Compared with the $Sb_2S_3/Sb_2(S, Se)_3$ film, the Sb 3d peaks of $Sb_2S_3/Sb_2(S, Se)_3$/P3HT shifted to lower binding energy (Figure 5c). The low binding energy suggested that the electron density around Sb increased, which could be ascribed to the interactions with electron-rich thiophene fractions [27].

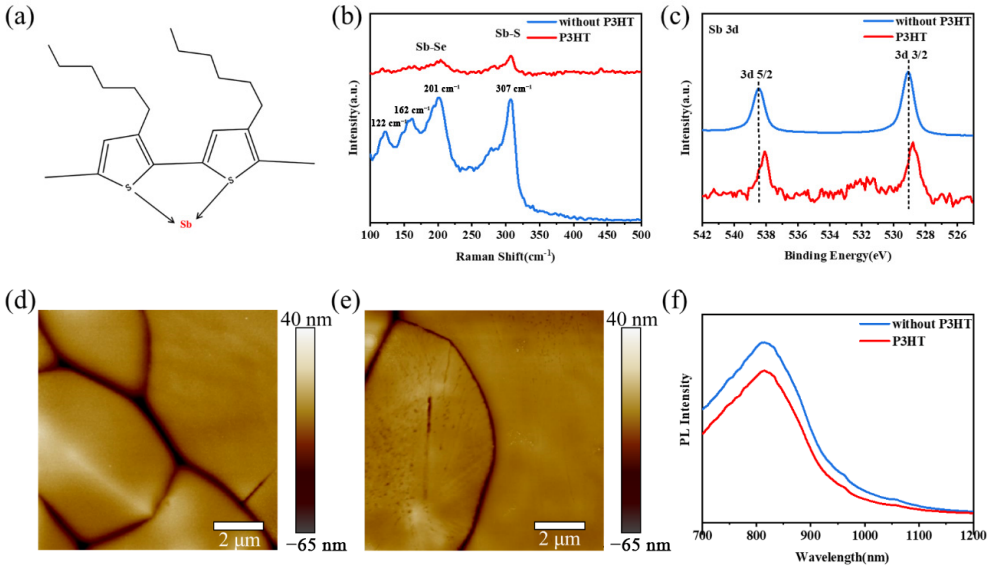

Figure 5. (**a**) Scheme of chelating interaction between P3HT and Sb. (**b**) Raman and (**c**) XPS spectra of the $Sb_2S_3/Sb_2(S, Se)$ and $Sb_2S_3/Sb_2(S, Se)_3$/P3HT films. AFM images of the (**d**) $Sb_2S_3/Sb_2(S, Se)_3$ and (**e**) $Sb_2S_3/Sb_2(S, Se)_3$/P3HT films. (**f**) Steady-state PL spectra of the $Sb_2S_3/Sb_2(S, Se)_3$ and $Sb_2S_3/Sb_2(S, Se)_3$/P3HT films.

Atomic force microscopy (AFM) was performed to observe the change in the morphology with and without a P3HT layer (Figure 5d,e). According to the AFM results, the roughness values (R_q) of the $Sb_2S_3/Sb_2(S, Se)_3$ and $Sb_2S_3/Sb_2(S, Se)_3$/P3HT are calculated to be 12.0 nm and 6.52 nm, respectively. Therefore, the deposition of the P3HT layer reduced the surface roughness of $Sb_2S_3/Sb_2(S, Se)_3$ films. The flat surface is believed to benefit the interfacial contact with the carbon electrode. In addition, the steady-state photoluminescence (PL) spectra showed that the PL intensity of $Sb_2S_3/Sb_2(S, Se)_3$ films was smaller than that of $Sb_2S_3/Sb_2(S, Se)_3$/P3HT films (Figure 5f). The quenched PL indicated that P3HT significantly enhanced hole extraction of $Sb_2S_3/Sb_2(S, Se)_3$ based solar cells [28,29].

To evaluate the influence of P3HT on PV performance, carbon-based $Sb_2S_3/Sb_2(S, Se)_3$ solar cells with and without P3HT were fabricated by depositing carbon electrodes on the $Sb_2S_3/Sb_2(S, Se)_3$ and $Sb_2S_3/Sb_2(S, Se)_3$/P3HT substrates. As depicted in Figure 6a, the carbon electrode closely contacts the P3HT layer, which is favorable for charge collection. In Figure 6b, the *J*–*V* curves showed that the solar cell with P3HT showed a champion PCE of 4.15%, with a V_{OC} of 0.536 V, J_{SC} of 15.37 mA·cm^{-2}, and FF of 0.504, while the solar cell without P3HT showed a much lower PCE of 2.76%, with a V_{OC} of 0.467 V, J_{SC} of 13.24 mA·cm^{-2} and FF of 0.447. The energy alignments of the solar cells with a structure of $SnO_2/CdS/Sb_2S_3/Sb_2(S, Se)_3$/P3HT/carbon are illustrated in Figure 6c [20,29,30]. The high HOMO of P3HT can effectively prevent electrons from entering P3HT, which remarkably suppressed the recombination at this interface and thus increased the PCE of solar cells.

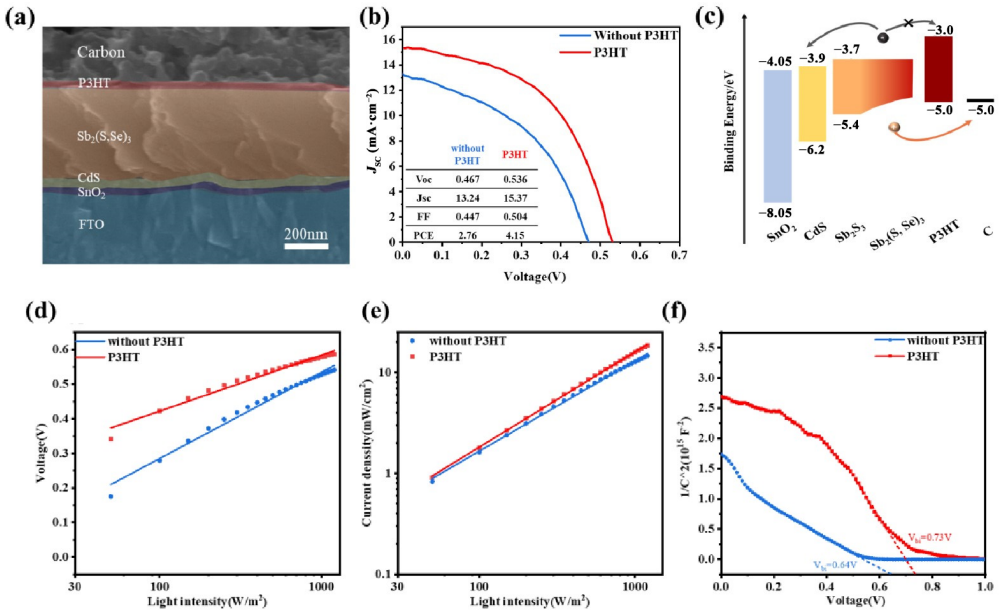

Figure 6. (**a**) Cross-sectional SEM image of the solar cell with P3HT. (**b**) *J*–*V* curves of the solar cells with and without P3HT. (**c**) Energy level diagrams of solar cells with a structure of SnO_2/CdS/Sb_2S_3/Sb_2(S, Se)$_3$/P3HT/carbon. Dependence of (**d**) V_{OC} and (**e**) J_{SC} under a different light intensity of the solar cells with and without P3HT. (**f**) Mott-Schottky plots were obtained at 10 kHz of the solar cells with and without P3HT.

Figure 6d shows the dependence of V_{OC} and J_{SC} on light intensity (I), which can be fitted by the following two equations [31].

$$V_{OC} = \frac{\varepsilon kTln(I)}{e} + constant \quad (1)$$

$$J_{SC} \propto I^{\alpha} \alpha \leq 1 \quad (2)$$

where k is the Boltzmann constant, T is the absolute temperature, e is the elementary charge, and ε/α are the ideality factors of a diode. The ε for the solar cells with and without P3HT was calculated to be 4.01 and 2.60, respectively, indicating the suppression of the monomolecular trap-assisted Shockley-Read-Hall (SRH) recombination with P3HT [32]. A linear dependence of J_{SC} on I is also found for both devices and the α values obtained are calculated to be 0.90 and 0.95 for the solar cells with and without P3HT (Figure 6e), respectively, which demonstrates that P3HT HTM enhanced charge separation and suppressed bimolecular recombination [18]. Mott–Schottky plots of the different solar cells were also collected. As shown in Figure 6f, the built-in potential (V_{bi}) for the pristine and P3HT devices is calculated to be about 0.64 V and 0.73 V, respectively. The larger V_{bi} would contribute to a higher driving force for efficient charge separation and a wider depletion region inhibiting the charge recombination, which is beneficial for achieving higher V_{OC} and FF, consistent with the *J*–*V* curves. All of the above characterizations are in good consistence with the performance difference between solar cells with and without P3HT.

3. Materials and Methods

3.1. Device Fabrication

Deposition of SnO_2 films: All devices were deposited on clean fluorine-doped tin oxide (FTO) glass. FTO glass was cleaned thoroughly in deionized water, ethyl alcohol, and isopropanol with the assistance of sonication. Prior to electron transport layer deposition, the substrates were subjected to UV/ozone treatment for 20 min at room temperature.

SnO_2 blocking layers were spin-coated onto FTO glass at 3000 rpm for 30 s, using SnO_2 colloidal dispersion. All processes were conducted in an ambient air atmosphere.

Deposition of CdS films: CdS thin films were then deposited by a chemical bath deposition (CBD) method. Next, 30 mL of 15 mM Cd $(NO_3)_2$ and 39 mL of ammonia water were mixed and stirred for 5 min. Then, 19.2 mL of 1.2 M thiourea and 210 mL of deionized water were added to the mixture and stirred for 2 min to get the precursor solution. Thereafter, the solution was heated and kept at 65 °C by using a water bath. FTO/SnO_2 substrates were sloped down in the precursor solution and maintained for 15 min. After the samples were taken out, a 20 mg/mL $CdCl_2$ solution was spin-coated onto the as-deposited CdS layer, followed by annealing at 400 °C for 10 min to get the final FTO/SnO_2/CdS samples. All processes were conducted in an ambient air atmosphere.

Deposition of Sb_2S_3 and $Sb_2(S, Se)_3$ films: All Sb_2S_3 and $Sb_2(S, Se)_3$ films were deposited by hydrothermal method.

For the deposition of the Sb_2S_3 films, 20 mM $KSbC_4H_4O_7{\cdot}0.5H_2O$ and 40 mM $Na_2S_2O_3{\cdot}5H_2O$ were dissolved in deionized water. The mixture was then put into the Teflon tank of autoclave and the FTO/SnO_2/CdS substrate was put into the above solution and heated to 135 °C and kept for 10 h using an oven. After cooling down to room temperature, the samples were taken out and washed with deionized water and ethyl alcohol. Then, they were annealed at 350 °C for 15 min in a glove box filled with N_2 (1.2–1.5 mbar).

For the deposition of $Sb_2(S, Se)_3$ films, 20 mM $KSbC_4H_4O_7{\cdot}0.5H_2O$ and 80 mM $Na_2S_2O_3{\cdot}5H_2O$ were dissolved in deionized water. After the two chemicals were dissolved, 4 mM of selenourea was added to the solution and stirred until it was well dissolved. The mixture was then put into the Teflon tank of autoclave and the FTO/SnO_2/CdS substrates were put into the above solution. The hydrothermal process was conducted by putting the solution in an oven at 135 °C and kept for 3 h. After cooling down to room temperature, the samples were taken out and washed with deionized water and ethyl alcohol. Then, they were annealed at 350 °C for 15 min in a glove box filled with N_2 (1.2–1.5 mbar).

For the deposition of $Sb_2S_3/Sb_2(S, Se)_3$ films, a two-step hydrothermal method was developed. Firstly, the Sb_2S_3 films were deposited by the above hydrothermal method and deposition duration was adjusted to 1 h, 2 h, 3 h, and 4 h. After the deposition of Sb_2S_3 films, $Sb_2(S, Se)_3$ films were also deposited by the hydrothermal method and the reaction duration was fixed to 2 h. After hydrothermal deposition, the above films were taken out and washed with deionized water and ethyl alcohol. Then, they were annealed at 350 °C for 15 min in a glove box filled with N_2 (1.2–1.5 mbar).

Deposition of P3HT films: P3HT solution was prepared by dissolving 10 mg/mL P3HT in chlorobenzene. The P3HT layer was deposited on the $Sb_2S_3/Sb2_(S, Se)_3$ films by spin-coating the P3HT solution at room temperature with 3000 rpm for 30 s. Finally, the deposited samples were annealed at 120 °C for 10 min. All processes were conducted in a glove box filled with N_2 (1.2–1.5 mbar).

Deposition of carbon electrodes: Carbon electrodes are deposited on different films by using a commercialized carbon paste that was purchased from Guangzhou Seaside Technology Co., Ltd. and was used without any treatment. The wet carbon layers were first painted on the targeted films at room temperature, which were then annealed at 120 °C for 30 min to form the final carbon electrode. All processes were conducted in a dry-air atmosphere.

3.2. Characterizations

XRD patterns were obtained on a Rigaku D/MAX-2500 X-ray diffractometer with an X-ray tube Cu Ka radiation. (λ =1.5406 Å). Ultraviolet-visible-infrared spectrophotometer absorption spectra were recorded on a Shimadzu UV-3600 ultraviolet-visible spectrometer. SEM images and EDS were obtained on a SUPRA55 SEM at an accelerating voltage of 10 kV. The surface roughness of the films was characterized by a Bruker Dimension ICON AFM. Raman spectroscopy was measured at room temperature using a Raman spectrometer (InVia, Renishaw Inc., Stonehouse, UK) equipped with a green laser (532 nm), and the

laser power and objective were 50 mW and 50×, respectively. The chemical states of the film surface were evaluated by an X-ray photoemission spectroscope (ESCALab250Xi). Steady-state PL spectra were recorded on a Nanolog FL3-2iHR (Horiba Jobin Yvon Ltd., Palaiseau, France) with an excitation wavelength of 635 nm.

The photovoltaic performance was tested under a solar light simulator (Newport Oriel Sol 3A, model number 94063A, AM 1.5 global filter) in an ambient air atmosphere. The light intensity was calibrated to 1 Sun (100 mW/cm^2) using an Oriel reference solar cell (monocrystalline silicon) and meter. The active area of cells was masked at around 6.25 mm^2. Current density-voltage (J–V) curves, the dependence of J_{SC} and V_{OC} on the light intensity, and Mott-Schottky curves were measured on a ZENNIUM pro electrochemical workstation (ZAHNER-Elektrik GmbH & Co., KG, Kronach, Germany) in an ambient air atmosphere.

4. Conclusions

We have developed a two-step hydrothermal deposition method to grow stacked $Sb_2S_3/Sb_2(S, Se)_3$ films with large grains and flat surfaces. By using such films in carbon-based $Sb_2(S, Se)_3$ solar cells without HTMs, a PCE of 2.76% was achieved. After employing P3HT as the HTM, energy level alignment at the hole contact was improved and charge extraction was significantly accelerated. As a result, the PCE of the solar cells with a structure of $SnO_2/CdS/Sb_2S_3/Sb_2(S, Se)_3/P3HT/carbon$ was promoted to 4.15%. The successful fabrication of solar cells with a structure of $SnO_2/CdS/Sb_2S_3/Sb_2(S, Se)_3/P3HT/carbon$ brings out a promising route to produce solar cells with cost-effective and stable materials.

Supplementary Materials: The following supporting information can be downloaded at: https://www.mdpi.com/article/10.3390/inorganics11040159/s1, Figure S1: SEM images of $Sb_2S_3/Sb_2(S, Se)_3$ films with different deposition durations of the Sb_2S_3 films. Figure S2: XRD patterns of the Sb_2S_3, $Sb_2(S, Se)_3$, $Sb_2S_3/Sb_2(S, Se)_3$ films. Figure S3: EDS element mappings of $Sb_2S_3/Sb_2(S, Se)_3$ films with the pre-deposition of Sb_2S_3 for 3 h. And Figure S4: Steady-state power output of $Sb_2S_3/Sb_2(S, Se)_3$ based solar cells with P3HT.

Author Contributions: Conceptualization, H.C., Y.D. and S.X.; methodology, Y.D., H.L., H.W. and Y.S.; formal analysis, W.L., X.X. and L.Z.; investigation, Y.D. and H.L.; writing—original draft preparation, Y.D.; writing—review and editing, H.C. and S.X.; visualization, Y.D.; supervision, H.C. and S.X.; funding acquisition, H.C. and S.X. All authors have read and agreed to the published version of the manuscript.

Funding: This research was funded by the National Natural Science Foundation of China (21875013 and 21905006), the Beijing Natural Science Foundation (No. 2182031), the Young Talent of "Zhuoyue" Program of Beihang University, Guangdong Provincial Science and Technology Plan (2021A0505110003), Guangdong Basic and Applied Basic Research Foundation (2020B1515120039), Shenzhen Peacock Plan (KQTD2016053015544057), Shenzhen Collaborative Innovation and Technology Program (2022378670) and Shenzhen Fundamental Research Program (JCYJ20200109110628172, JCYJ20190808163201831).

Data Availability Statement: Not applicable.

Conflicts of Interest: The authors declare no conflict of interest.

References

1. Green, M.A.; Dunlop, E.D.; Hohl-Ebinger, J.; Yoshita, M.; Kopidakis, N.; Bothe, K.; Hinken, D.; Rauer, M.; Hao, X. Solar Cell Efficiency Tables (Version 60). *Prog. Photovolt. Res. Appl.* **2022**, *30*, 687–701. [CrossRef]
2. Hu, X.; Tao, J.; Wang, R.; Wang, Y.; Pan, Y.; Weng, G.; Luo, X.; Chen, S.; Zhu, Z.; Chu, J.; et al. Fabricating over 7%-Efficient $Sb_2(S,Se)_3$ Thin-Film Solar Cells by Vapor Transport Deposition Using Sb_2Se_3 and Sb_2S_3 Mixed Powders as the Evaporation Source. *J. Power Sources* **2021**, *493*, 229737. [CrossRef]
3. Zhou, Y.; Wang, L.; Chen, S.; Qin, S.; Liu, X.; Chen, J.; Xue, D.J.; Luo, M.; Cao, Y.; Cheng, Y.; et al. Thin-Film Sb_2Se_3 Photovoltaics with Oriented One-Dimensional Ribbons and Benign Grain Boundaries. *Nat. Photonics* **2015**, *9*, 409–415. [CrossRef]
4. Tang, R.; Wang, X.; Lian, W.; Huang, J.; Wei, Q.; Huang, M.; Yin, Y.; Jiang, C.; Yang, S.; Xing, G.; et al. Hydrothermal Deposition of Antimony Selenosulfide Thin Films Enables Solar Cells with 10% Efficiency. *Nat. Energy* **2020**, *5*, 587–595. [CrossRef]

5. Wen, X.; Chen, C.; Lu, S.; Li, K.; Kondrotas, R.; Zhao, Y.; Chen, W.; Gao, L.; Wang, C.; Zhang, J.; et al. Vapor Transport Deposition of Antimony Selenide Thin Film Solar Cells with 7.6% Efficiency. *Nat. Commun.* **2018**, *9*, 2179. [CrossRef]
6. Jiang, C.; Zhou, J.; Tang, R.; Lian, W.; Wang, X.; Lei, X.; Zeng, H.; Zhu, C.; Tang, W.; Chen, T. 9.7%-Efficient $Sb_2(S,Se)_3$ Solar Cells with a Dithieno [3,2-: B: 2′,3′-d] Pyrrole-Cored Hole Transporting Material. *Energy Environ. Sci.* **2021**, *14*, 359–364. [CrossRef]
7. Wang, W.; Cao, Z.; Wu, L.; Liu, F.; Ao, J.; Zhang, Y. Remarkable Sb_2Se_3 Solar Cell with a Carbon Electrode by Tailoring Film Growth during the VTD Process. *ACS Appl. Energy Mater.* **2021**, *4*, 13335–13346. [CrossRef]
8. Gratia, P.; Magomedov, A.; Malinauskas, T.; Daskeviciene, M.; Abate, A.; Ahmad, S.; Grätzel, M.; Getautis, V.; Nazeeruddin, M.K. Methoxydiphenylamin-Substituiertes Carbazol-Zwillingsderivat: Ein Effizienter Organischer Lochleiter Für Perowskit-Solarzellen. *Angew. Chem.* **2015**, *127*, 11571–11575. [CrossRef]
9. Xu, B.; Bi, D.; Hua, Y.; Liu, P.; Cheng, M.; Grätzel, M.; Kloo, L.; Hagfeldt, A.; Sun, L. A Low-Cost Spiro[Fluorene-9,9′-Xanthene]-Based Hole Transport Material for Highly Efficient Solid-State Dye-Sensitized Solar Cells and Perovskite Solar Cells. *Energy Environ. Sci.* **2016**, *9*, 873–877. [CrossRef]
10. Jung, E.H.; Jeon, N.J.; Park, E.Y.; Moon, C.S.; Shin, T.J.; Yang, T.Y.; Noh, J.H.; Seo, J. Efficient, Stable and Scalable Perovskite Solar Cells Using Poly(3-Hexylthiophene). *Nature* **2019**, *567*, 511–515. [CrossRef]
11. Rezaee, E.; Liu, X.; Hu, Q.; Dong, L.; Chen, Q.; Pan, J.-H.; Xu, Z.-X. Dopant-Free Hole Transporting Materials for Perovskite Solar Cells. *Sol. RRL* **2018**, *2*, 1800200. [CrossRef]
12. Kim, Y.; Cook, S.; Tuladhar, S.M.; Choulis, S.A.; Nelson, J.; Durrant, J.R.; Bradley, D.D.C.; Giles, M.; McCulloch, I.; Ha, C.S.; et al. A Strong Regioregularity Effect in Self-Organizing Conjugated Polymer Films and High-Efficiency Polythiophene:Fullerene Solar Cells. *Nat. Mater.* **2006**, *5*, 197–203. [CrossRef]
13. Osedach, T.P.; Andrew, T.L.; Bulović, V. Effect of Synthetic Accessibility on the Commercial Viability of Organic Photovoltaics. *Energy Environ. Sci.* **2013**, *6*, 711–718. [CrossRef]
14. Xiao, S.; Qian, W.; Yang, S. Interfaced Structures between Halide Perovskites: From Basics to Construction to Optoelectronic Applications. *Adv. Energy Mater.* **2022**, *13*, 2201472. [CrossRef]
15. Li, G.; Gao, X. Low-Cost Counter-Electrode Materials for Dye-Sensitized and Perovskite Solar Cells. *Adv. Mater.* **2020**, *32*, 1806478. [CrossRef]
16. Liu, T.; Wang, Z.; Lou, L.; Xiao, S.; Zheng, S.; Yang, S. Interfacial Post-Treatment for Enhancing the Performance of Printable Carbon-Based Perovskite Solar Cells. *Sol. RRL* **2020**, *4*, 1900278. [CrossRef]
17. Qian, W.; Xu, X.; Wang, J.; Xu, Y.; Chen, J.; Ge, Y.; Chen, J.; Xiao, S.; Yang, S. An Aerosol-Liquid-Solid Process for the General Synthesis of Halide Perovskite Thick Films for Direct-Conversion X-ray Detectors. *Matter* **2021**, *4*, 942–954. [CrossRef]
18. Zhang, K.; Wang, Z.; Wang, G.; Wang, J.; Li, Y.; Qian, W.; Zheng, S.; Xiao, S.; Yang, S. A Prenucleation Strategy for Ambient Fabrication of Perovskite Solar Cells with High Device Performance Uniformity. *Nat. Commun.* **2020**, *11*, 1006. [CrossRef]
19. Kumar, A.; Kumar, V.; Romeo, A.; Wiemer, C.; Mariotto, G. Raman Spectroscopy and In Situ XRD Probing of the Thermal Decomposition of Sb_2Se_3 Thin Films. *J. Phys. Chem. C* **2021**, *125*, 19858–19865. [CrossRef]
20. Zhang, Y.; Li, J.; Jiang, G.; Liu, W.; Yang, S.; Zhu, C.; Chen, T. Selenium-Graded $Sb_2(S_{1-x}Se_x)_3$ for Planar Heterojunction Solar Cell Delivering a Certified Power Conversion Efficiency of 5.71%. *Sol. RRL* **2017**, *1*, 1700017. [CrossRef]
21. He, R.; Zuo, C.; Ren, S.; Zhao, D.; Ding, L. Low-Bandgap Sn–Pb Perovskite Solar Cells. *J. Semicond.* **2021**, *42*, 060202. [CrossRef]
22. Dionigi, C.; Calabrese, G.; Ruani, G.; Milita, S. Short-Chain Acid Additives to Control PbI_2 Crystallization in Hybrid Perovskite Films. *Inorganics* **2022**, *10*, 114. [CrossRef]
23. Dou, J.; Bai, Y.; Chen, Q. Challenges of Lead Leakage in Perovskite Solar Cells. *Mater. Chem. Front.* **2022**, *6*, 2779–2789. [CrossRef]
24. Li, W.; Fan, J.; Ding, L. Multidimensional Perovskites Enhance Solar Cell Performance. *J. Semicond.* **2021**, *42*, 020201. [CrossRef]
25. Chen, G.J.; Tang, R.; Chen, S.; Zheng, Z.H.; Su, Z.H.; Ma, H.L.; Zhang, X.H.; Fan, P.; Liang, G.X. Crystal Growth Promotion and Defect Passivation by Hydrothermal and Selenized Deposition for Substrate-Structured Antimony Selenosulfide Solar Cells. *ACS Appl. Mater. Interfaces* **2022**, *14*, 31986–31997. [CrossRef]
26. Turkoglu, F.; Ekren, M.E.; Cantas, A.; Yakinci, K.; Gundogan, H.; Koseoglu, H.; Aygun, G.; Ozyuzer, L. Structural and Optical Characteristics of Antimony Selenosulfide Thin Films Prepared by Two-Step Method. *J. Korean Phys. Soc.* **2022**, *81*, 278–284. [CrossRef]
27. Sulas, D.B.; London, A.E.; Huang, L.; Xu, L.; Wu, Z.; Ng, T.N.; Wong, B.M.; Schlenker, C.W.; Azoulay, J.D.; Sfeir, M.Y. Preferential Charge Generation at Aggregate Sites in Narrow Band Gap Infrared Photoresponsive Polymer Semiconductors. *Adv. Opt. Mater.* **2018**, *6*, 1701138. [CrossRef]
28. Mu, F.; Liu, Z.; Zi, W.; Cao, Y.; Lu, X.; Li, Y.; Zhao, Z.; Xiao, Z.; Cheng, N. CZTS Nanoparticles as an Effective Hole-Transport Layer for Sb_2Se_3 Thin-Film Solar Cells. *Sol. Energy* **2021**, *226*, 154–160. [CrossRef]
29. Wang, G.; Dong, W.; Gurung, A.; Chen, K.; Wu, F.; He, Q.; Pathak, R.; Qiao, Q. Improving Photovoltaic Performance of Carbon-Based $CsPbBr_3$ Perovskite Solar Cells by Interfacial Engineering Using P3HT Interlayer. *J. Power Sources* **2019**, *432*, 48–54. [CrossRef]
30. Makin, F.; Alzahrani, D.; Alam, F.; Tuna, F.; Lewis, D.J. Testing the Efficacy of the Synthesis of Iron Antimony Sulfide Powders from Single Source Precursors. *Inorganics* **2021**, *9*, 61. [CrossRef]

31. Lenes, M.; Morana, M.; Brabec, C.J.; Blom, P.W.M. Recombination-Limited Photocurrents in Low Bandgap Polymer/Fullerene Solar Cells. *Adv. Funct. Mater.* **2009**, *19*, 1106–1111. [CrossRef]
32. Duan, J.; Zhao, Y.; He, B.; Tang, Q. Simplified Perovskite Solar Cell with 4.1% Efficiency Employing Inorganic $CsPbBr_3$ as Light Absorber. *Small* **2018**, *14*, 1704443. [CrossRef]